

See discussions, stats, and author profiles for this publication at: <https://www.researchgate.net/publication/51845779>

Dynamic Evolution of Supported Metal Nanocatalyst/Carbon Structure during Single-Walled Carbon Nanotube Growth

ARTICLE *in* ACS NANO · DECEMBER 2011

Impact Factor: 12.88 · DOI: 10.1021/nn204215c · Source: PubMed

CITATIONS

31

READS

46

4 AUTHORS, INCLUDING:



[Diego Gomez-Gualdrón](#)

Northwestern University

23 PUBLICATIONS 283 CITATIONS

[SEE PROFILE](#)



[Javier Alvarado](#)

Instituto Tecnológico de Celaya

26 PUBLICATIONS 212 CITATIONS

[SEE PROFILE](#)



[Perla B. Balbuena](#)

Texas A&M University

245 PUBLICATIONS 5,637 CITATIONS

[SEE PROFILE](#)

Dynamic Evolution of Supported Metal Nanocatalyst/Carbon Structure during Single-Walled Carbon Nanotube Growth

Diego A. Gómez-Gualdrón,[†] Gilbert D. McKenzie,[†] Juan F. J. Alvarado,[‡] and Perla B. Balbuena^{†,*}

[†]Department of Chemical Engineering and Material Sciences and Engineering Program, Texas A&M University, College Station, Texas 77843, United States, and

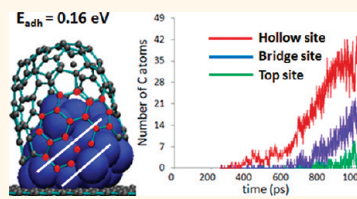
[‡]Departamento de Ingeniería Química, Instituto Tecnológico de Celaya, Celaya, Gto 38010, México

For about two decades, carbon nanotubes have been envisioned as one of the most promising materials in nanotechnology.^{1–3} In particular, SWCNTs possess a number of astounding electrical, optical, and mechanical properties⁴ with the potential to revolutionize several fields such as electronics, materials science, and medicine through their implementation in sophisticated devices (e.g., single-electron transistors),⁵ nanocomposite structures (e.g., nanotubes in polymeric matrices),⁶ and new diagnosis and therapeutic procedures (e.g., nanotube-based biosensors).⁷ Geometrically, a carbon nanotube is obtained by bringing together two points in a graphene sheet, rolling it into tubular form. Selection of different points results in different helical patterns of the nanotube wall.⁸ A way to describe this helicity is with the *chiral angle*, which spans values from 0 to 30°. The lowest value corresponds to a *zigzag* nanotube and the highest to an *armchair* nanotube. Interestingly, the properties of the nanotubes are found to depend on their chiral angle and their diameter (or alternatively on their chiral indexes (*n,m*)),⁸ opening the possibility of selecting the most appropriate type of nanotube for a given application (e.g., selecting a given band gap). Unfortunately, nanotubes are usually synthesized in bundles^{9,10} containing different *chiralities*, where their outstanding properties are lost. Thus additional steps are required to separate the nanotubes,^{11,12} increasing the production cost and decreasing the viability of application.

Accordingly, there is a huge interest in controlling the chirality of the nanotubes *during* synthesis to allow the exploitation of carbon-nanotube-based technologies. Throughout the past decade, some processes such as CoMoCAT (majority of (6,5) and (7,5) nanotubes)¹³ were known to

ABSTRACT Single-walled carbon nanotubes (SWCNTs) have outstanding properties that depend on structural features such as their chirality. Thus, developing a strategy to control chirality during SWCNT synthesis is critical for the exploitation of nanotube-

based technologies in fields such as electronics and biomedicine. In response to this need, tuning the nanocatalyst structure has been envisioned as a means to control the nanotube structure. We use reactive classical molecular dynamics to simulate nanotube growth on supported Ni₃₂, Ni₈₀, and Ni₁₆₀ nanoparticles at various metal/support interaction strengths (E_{adh}). The initial carbon ring formation is shown to correlate to the nanoparticle surface structure, demonstrating the existence of a “template effect” through a dominant occupation of hollow sites. The E_{adh} strength alters the dynamic/structural behavior of the nanoparticle, in turn influencing the interplay between nanotube and nanoparticle structures. For example, the contact region between the nanoparticle surface and the growing nanotube decreases as E_{adh} increases because capillary forces that raise the metal into the nanotube are counteracted by the strong metal/support interaction. The nanoparticle mobility decreases as E_{adh} increases, eliminating a possible inverse template effect but hindering defect annealing in detriment of the nanotube/nanoparticle structural correlation. On the other hand, the contact between the nanoparticle and the nanotube increases with nanoparticle size. However, the heterogeneity of the nanoparticle structure increases with size, reducing the structural correlation. These results suggest that an appropriate combination of nanoparticle size and strength of the catalyst/support interaction may enhance the desired template effect and bias formation of specific nanotube chiralities.



KEYWORDS: reactive molecular dynamics · template effect · nanotube chirality · selective nanotube synthesis

produce SWCNTs with a relatively narrow chiral distribution. This process used a bimetallic cobalt–molybdenum catalyst on different supports (SiO₂ and MgO), wherein change in the support was one of the factors shown to alter the chiral distribution. Using cobalt supported on TUD-1 (an ordered mesoporous silica),¹⁴ a majority of (9,8) nanotubes were produced instead,¹⁵ also suggesting that the catalyst support can indirectly influence nanotube chirality. In addition

* Address correspondence to
balbuena@tamu.edu.

Received for review November 1, 2011
and accepted December 1, 2011.

Published online December 01, 2011
10.1021/nn204215c

© 2011 American Chemical Society

to changing the support, the catalyst/support interaction has also been changed by using different metals. For instance, He *et al.* produced majority of (6,5) using both cobalt¹⁶ and nickel,¹⁷ but the abundance of secondary (7,5), (7,6), and (8,4) was altered by the use of either metal. Similarly, altering the interaction with the support using a bimetallic Fe–Cu catalyst, He *et al.* were able to produce (6,5) majority on a MgO catalyst,¹⁸ overcoming the inactivity of monometallic Cu and the selectivity of Fe toward multiwalled carbon nanotube formation on that substrate.

On the other hand, in recent years, theoretical and experimental work has suggested that the structure of the nanoparticle directly affects the resulting chiral distribution. For instance, Zhu *et al.*¹⁹ used HRTEM images to show a correlation between the chirality of the nanotube and the structure of the catalytic nanoparticle. Also, Chiang and Sankaran²⁰ demonstrated that structural changes in bimetallic Ni–Fe nanoparticles caused changes in the resulting chiral distribution. On the other hand, Harutyunyan *et al.*²¹ showed that the production of ~90% of metallic nanotubes was connected with a specific shape adopted by the Fe nanocatalyst during catalyst preparation. Similarly, in previous work, we used various theoretical methods to perform simulations aimed to prove the nanoparticle template effect hypothesis.²² However, a major concern is the occurrence of an inverse template effect which results from the much stronger C–C bond in comparison to C–M and M–M bonds. Moreover, some recent experiments^{23,24} have shown the restructuring of the nanoparticle during nanotube growth, thus suggesting the liquid-like state of the nanoparticle as a possible obstacle to the use of the nanoparticle structure for controlling the nanotube chirality. Nevertheless, it is possible that through a careful selection of catalyst material, support material, nanoparticle size, and temperature—to mention a few factors—an adequate interplay among these factors can create the necessary conditions for the template effect to occur.

In this work, our goal is to use our simulations as a theoretical microscope to carefully investigate the dynamics between carbon and metal at the atomistic level, while trying to understand the influence (or lack thereof) of the nanoparticle structure on the nascent carbon structure(s). Thus, to explore the relation between the structure of the nascent nanotube and that of the catalytic nanoparticle at different conditions, we simulate the growth of carbon nanotubes using various nanoparticle/support interaction strengths and three different nanoparticle sizes. Five simulations are performed at each condition to account for the statistical nature of the nanotube growth. First, the simulation trajectories are carefully analyzed to determine general trends common to three nanoparticle sizes and various nanoparticle/support interaction strengths. Second, the chiral angle θ_c at the end of the simulations is determined to be either high (near-armchair) or low

(near-zigzag), thus allowing one to evaluate whether a connection of chirality with the nanoparticle size, shape, or nanoparticle/support interaction exists. We follow with an analysis of the dynamics connecting the nanoparticle structure and the nascent carbon structures at the nucleation stage. This is done with the purpose of understanding epitaxial effects between metal and carbon and structural evolution of the metal nanoparticle at typical conditions of temperature and pressure of the synthesis. This analysis is carried out by determining the type of sites on the nanoparticle surface preferentially occupied by carbon atoms, while attempting to evaluate the extent at which the geometry of early carbon structures is influenced by the continuously evolving nanoparticle surface. This is analyzed across the different simulation conditions to find whether a “template effect” or an “inverse template effect” appears to dominate at the nucleation stage. We then extend our analysis to later times in the simulation trajectories to determine whether a correlation between the nanoparticle structure and the nanotube exists once factors such as lattice mismatching and lattice defects start to play a more significant role. We also study how the dynamic evolution of the nanoparticle structure may affect the existence of such correlation for different simulation conditions.

We use a classical reactive force field²⁵ that allows performing a comparatively large number of simulations, while successfully modeling nanotube growth.^{26–30} This allows somewhat accounting for the statistical nature of nanotube growth due to high temperature, different initial catalyst structures, and different adsorption sites. Thus, we expect our simulations to complement other more rigorous, but computationally more demanding, theoretical approaches.^{31–36} On the other hand, our force field readily permits modification of factors such as metal–carbon, carbon–support, and metal–support interaction strengths, thus enabling an extensive study on how different conditions affect the nanotube growth.^{37–39}

RESULTS AND DISCUSSION

General Growth Trends. Inspection of 75 simulation trajectories shows the nanotube growth to occur through the following steps: (1) carbon dissolution into the metal nanocatalyst particle; (2) carbon segregation to the nanoparticle surface; (3) formation of carbon nanostructures on the metal surface identified as (a) chains, (b) isolated rings (usually branched), and (c) concatenated rings (usually branched); (4) “merging” of carbon nanostructures to form a nanotube cap; (5) lifting-off of the nanotube cap; and (6) incorporation of carbon to the nanotube rim/nanoparticle surface interface (length increase). In general, the onset of chain formation occurs earlier than that for ring formation, while the onset for ring formation occurs earlier than that for concatenated ring formation. Nevertheless, the onset of a latter substage does not necessarily coincide with the end of an earlier substage

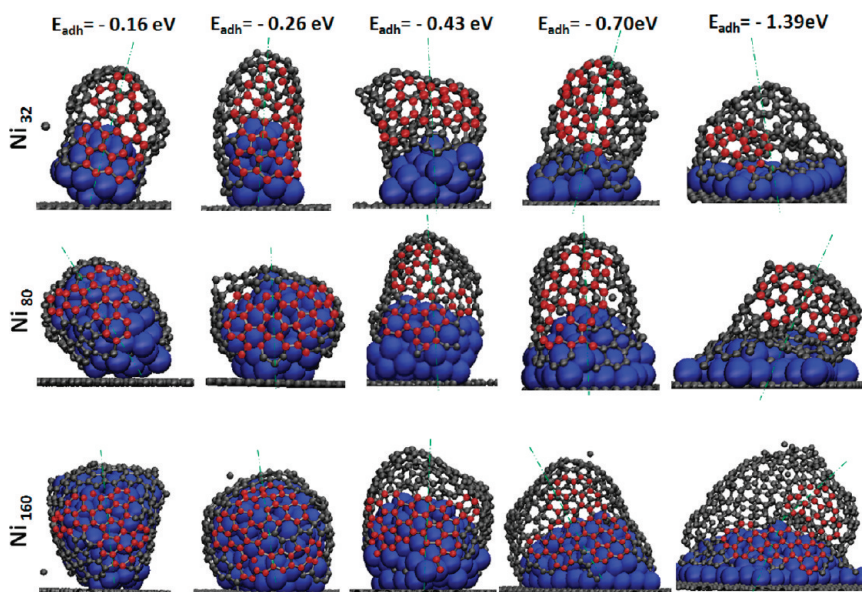


Figure 1. Snapshots after 5.00 ns of simulated growth showing the nascent nanotube structure (red and gray atoms) on supported metallic nanoparticle (blue atoms). The metal/substrate interaction strength increases from left to right, while the nanoparticle size increases from top to bottom; the annealing time before growth was 0.10 ns. Carbon atoms used in assessing the chiral angle appear in red. Green dash-dotted lines are used to indicate the axial direction.

since in a number of instances the formation of chains (or rings) may occur after some rings (or concatenated rings) have already been formed. This sort of scenario was more apparent for larger nanoparticle sizes due to the surface area increase. Additionally, formation of rings (or concatenated rings) was observed while the formation of chains (or rings) was dominant, but such rings (or concatenated rings) appeared to be less stable—having lifetimes of a few picoseconds. On the other hand, as the metal–substrate interaction E_{adh} decreases, the number of carbon structures (chains, rings, and concatenated rings) on the nanoparticle surface for a particular surface carbon concentration increases. For example, on a Ni_{32} particle initially annealed for 0.5 ns, 15 carbon atoms are found to form two chains (C_{11} and C_4) when $E_{\text{adh}} = -1.39$ eV, whereas the same number of atoms form three chains (C_6 , C_5 , and C_4) at a weaker $E_{\text{adh}} = -0.16$ eV for the same initial conditions of the nanoparticle. This could be related to a higher mobility of the metal atoms at weaker E_{adh} that may increase the number of favorable nucleation points on the nanoparticle surface. We come back to this point in a later section when discussing the relative occupancies of surface sites by C atoms.

Snapshots in Figure 1 illustrate typical appearances of nascent nanotubes after 5 ns of simulation. Although the presented snapshots are only for one set of initial conditions ($t_a = 0.10$ ns), representative trends observed in the analysis of all simulation trajectories can be summarized as follows: (1) A correlation between nanotube diameter (d) and nanoparticle size is apparent^{13,40–42} with the change in particle size from Ni_{32} through Ni_{160} (at constant E_{adh}), and with

the variation of E_{adh} from -0.16 through -1.39 eV (at constant particle size). (2) Cap lift-off occurs faster when E_{adh} is stronger. As cap lift-off starts, the separation between the nanotube cap and the nanoparticle becomes apparent, with the nanotube rim region keeping the contact with the nanocatalyst. Carbon atoms are incorporated to the nanotube through this contact region, thus allowing the growth of the nanotube via a root-growth mechanism.⁴³ It was apparent that the number of carbon atoms involved in this contact region decreases as E_{adh} increases. It is noteworthy that regions of the nanotube not contacting the nanoparticle do not show major restructuration during growth (*i.e.*, bond rearrangement seldom occurs), thus the probability of healing existing defects or creating new ones appears to be very low. On the other hand, the contact region is observed to continuously reconstruct mediated by the dynamics of metal atoms, thus facilitating defect healing and formation. This is in agreement with previous studies suggesting the importance of the metal for defect annealing.^{35,44} These phenomena are revisited in a later section discussing its impact for controlling the nanotube structure. During cap lift-off, the nanoparticle is observed to periodically change its shape. The effect is more noticeable for weak E_{adh} values, as revealed by the change in height of the nanoparticle mass center (NP_{mc}), with respect to the substrate position, during the simulation. For strong E_{adh} , the cap-lift occurs as the height of the NP_{mc} decreases, involving flattening of the nanoparticle. This process has been recently discussed from an energetic point of view.⁴⁵ The acceleration of cap lift-off at stronger E_{adh} occurs because a stronger attraction of the substrate to the

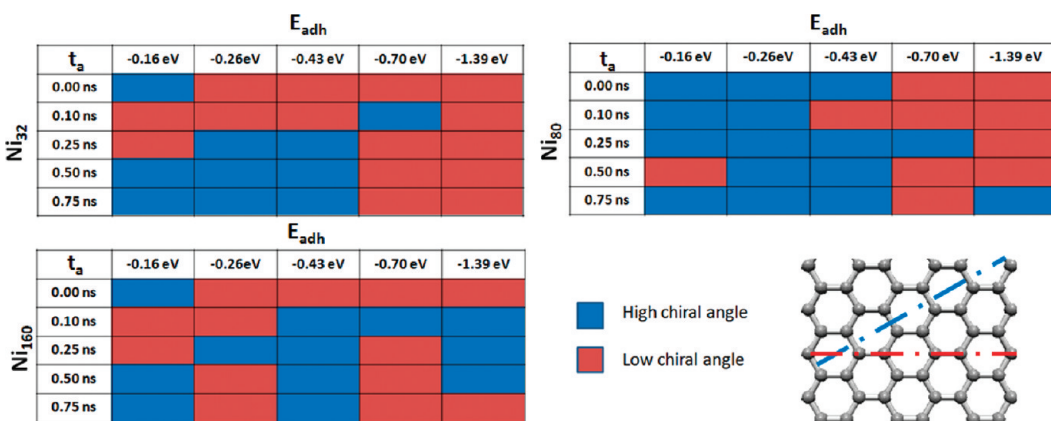


Figure 2. Schematics showing the classification of the nascent nanotube into a high ($\sim 30^\circ$) or a low ($\sim 0^\circ$) chiral angle structure after 5.00 ns of simulated growth. Each cell corresponds to a particular set of metal/substrate interaction strength (E_{adh}), catalyst size, and annealing time (t_a) before growth (hence different initial catalyst structure). The chiral angle is determined according to the relative orientation of the nanotube graphene network (red atoms in Figure 1) and the axial direction (green dash-dotted line in Figure 1) according to the schematics in the lower-right corner.

metal atoms allows counteracting the capillary forces that tend to raise the metal into the nanotube.^{23,24} For weak E_{adh} , when the cap starts lifting-off, the (relatively) “fluid” nanoparticle elongates in the direction of growth, thus increasing the time that the cap and the nanoparticle are in contact. Moreover, the wetting angle ω of the nanoparticle on the substrate is always larger when growth is occurring, in agreement with a growth-induced effect. In a previous study,³⁹ it was shown that such effect can be as strong as to detach the nanoparticle from the substrate as occurs for a tip-growth mechanism.⁴⁶ (3) A stronger E_{adh} typically results in lower angles (φ_G) of the nanotube growth direction (axial direction) with respect to the substrate, whereas weaker E_{adh} strengths result in variable φ_G (*i.e.*, growth direction oscillates during the simulation), and moderate E_{adh} typically results in upright growth ($\varphi_G \sim 90^\circ$). (4) Although the nanotubes grown during the simulation possess a number of defects, typically pentagonal and heptagonal rings, it is possible to recognize defect-free regions in their walls large enough to determine whether their chiral angle is low ($0^\circ < \theta_c < 15^\circ$) or high ($15^\circ < \theta_c < 30^\circ$). We recognize that defect healing could somewhat alter θ_c and d , thus we refrain from determining the exact (n,m) indexes, from their connection to θ_c and d , and rather focus our analysis on whether near-zigzag (low θ_c) or near-armchair (high θ_c) nanotubes are favored for a particular combination of nanoparticle size and E_{adh} . It is noted that, for a particular simulation, the region highlighted in Figure 1 is not the only defect-free region on the nanotube, but it is selected to show the relative orientation of the nanotube wall with respect to the surface and the nanotube axial direction used in the characterization of θ_c summarized in Figure 2.

Chirality Trends. Varying the pregrowth nanoparticle annealing time, t_a , results in different initial catalyst

structures to simulate the nanotube growth on Ni_{32} , Ni_{80} , and Ni_{160} nanoparticles at various values of E_{adh} . However, due to the relatively short annealing times, the difference among initial structures for a particular combination of catalyst size and E_{adh} is rather subtle; for instance, their density profiles are similar. Thus, the main purpose of evaluating different t_a values was to introduce higher statistical significance to the chiral angle analysis. From the data in Figure 2, the following observations are drawn: (1) relatively weak metal–substrate interaction strengths ($-0.16 \text{ eV} \leq E_{\text{adh}} \leq -0.43 \text{ eV}$) tend to favor near-armchair nanotubes for the smaller particle sizes (Ni_{32} and Ni_{80}) for values. In this E_{adh} range, 60.0% of the Ni_{32} simulations resulted in near-armchair nanotubes and 40.0% in near-zigzag nanotubes. Also, within this E_{adh} range, 83.3% of the simulations with shorter pregrowth annealing times ($t_a \leq 0.1 \text{ ns}$) resulted in near-zigzag nanotubes, and 88.8% of the simulations with larger pregrowth annealing times ($t_a \geq 0.25 \text{ ns}$) resulted in near-armchair nanotubes. (2) In contrast, at higher metal–substrate interaction strengths ($-0.70 \text{ eV} \leq E_{\text{adh}} \leq -1.39 \text{ eV}$), 90.0% of the simulations using Ni_{32} resulted in near-zigzag nanotubes. It must be noted that the quality of the nanotubes produced in this range was much lower than those produced at lower values of E_{adh} ; this aspect is further discussed in a later section when referring to the interplay between metal surface reorganization and carbon nanostructure rearrangements. (3) It is also apparent that some of the chirality trends observed for the smallest Ni_{32} are better defined in the intermediate sized Ni_{80} nanoparticle. For instance, for Ni_{80} , 86.6% of simulations in the $-0.16 \text{ eV} \leq E_{\text{adh}} \leq -0.43 \text{ eV}$ yielded near-armchair nanotubes, and in the $-0.70 \text{ eV} \leq E_{\text{adh}} \leq -1.39 \text{ eV}$ range, 80.0% resulted in near-zigzag nanotubes. (4) In contrast to Ni_{32} , no connection was found between the annealing times t_a and the resulting chiral angle for Ni_{80} possibly due to the lesser

impact of a particular annealing time on the structure of the intermediate sized Ni₈₀ compared to the smaller Ni₃₂. (5) The trends observed for Ni₃₂ and Ni₈₀ disappeared in the simulations of the larger Ni₁₆₀ nanoparticle where a clear chirality trend could not be found. For example, 53.3% of the simulations in the $-0.16 \text{ eV} \leq E_{\text{adh}} \leq -0.43 \text{ eV}$ range produced near-armchair nanotubes, and 60.0% of the simulations in the $-0.70 \text{ eV} \leq E_{\text{adh}} \leq -1.39 \text{ eV}$ range produced near-zigzag nanotubes. These observations suggest that increasing the nanoparticle size beyond a certain size could be detrimental for controlling the nanotube chiral angle since the distribution for Ni₁₆₀ presented a larger random character than those for Ni₃₂ and Ni₈₀. It must be noted that the set of (n,m) indexes that fit a particular nanotube diameter d increases in size as d increases. On the other hand, our simulations reveal that the final nanotube diameters were 0.2–0.4 nm larger than their corresponding nanoparticle. Accordingly, since Ni₁₆₀ has a larger diameter than Ni₈₀ and Ni₃₂, there is a larger number of (n,m) nanotubes potentially fitting Ni₁₆₀ in comparison to either Ni₃₂ or Ni₈₀, thus increasing the difficulty to impose chirality control.^{13,40} As a quantitative example, we note that the final average diameters for Ni₃₂, Ni₈₀, and Ni₁₆₀ for $E_{\text{adh}} \leq -0.26 \text{ eV}$ were found to be ~ 0.5 , ~ 0.9 , and ~ 1.2 nm, whereas their corresponding nanotubes were found to be ~ 0.9 , ~ 1.1 , and ~ 1.5 nm in diameter. On the basis of these diameters,⁴ the number of (n,m) nanotubes fitting a particular nanoparticle approaches seven for Ni₃₂, nine for Ni₈₀, and 13 for Ni₁₆₀, which implies an increase of 28% from Ni₃₂ to Ni₈₀, but one of 85% from Ni₃₂ to Ni₁₆₀.

A potential scenario is proposed linking the structures of the nascent nanotube and that of the evolving nanoparticle,^{19–22} where subtle differences in the structural behavior of Ni₁₆₀ compared to Ni₈₀ and Ni₃₂ could hinder the appearance of chiral distribution trends for the largest nanoparticle. For instance, as the nanoparticle size increases it is easier to detect (on the same nanoparticle) surface regions with different structural and dynamic behavior facilitated by the increased surface area and the high reaction temperature. In particular, sometimes it is noted a desynchronization in the orientation of neighbor surface “domains”, which is disadvantageous under the premise that the orientation of the nanoparticle surface could be connected to the nanotube chirality through epitaxial matching. This matching has been proposed to occur between the energetically favored (111) facets in fcc nanoparticles and the hexagonal lattice of the nanotube wall.^{19,22,47–49} Since, for a particular simulation time, the Ni₁₆₀ surface often shows neighbor (111) domains with conflicting orientation, the metal surface influence on the nanotube structure is unclear. We emphasize that although conflicting regions also are observed for Ni₈₀ and Ni₃₂ the ratio of desynchronized/synchronized regions is perceived to be smaller.

On the basis of the previous discussion, it is interesting to note that the simulations of Ni₈₀ presented somewhat more defined trends than the Ni₃₂ ones. Although this could be an artifact of the relatively small population sample (five simulations for each nanoparticle size and E_{adh}), it could also suggest that a moderately small nanoparticle could be optimal for chirality control.^{13,15,20} It is possible that although the number of (n,m) nanotubes fitting Ni₃₂ is 23% smaller than that for Ni₈₀, it is more difficult for the smallest nanoparticle to clearly impose its structure on the nascent nanotube. For instance, for the smallest particle and relatively weak $E_{\text{adh}} \leq -0.43 \text{ eV}$, the nanoparticle diameter is within the 0.5–0.8 nm range, wherein other factors such as curvature energies can have an important effect on the nanotube.^{38,50} On the other hand, although for $E_{\text{adh}} \geq -0.70 \text{ eV}$ the diameter is within the 0.9–1.1 nm range, the contact between the nanotube wall and the nanoparticle decreases since cap lift-off is accelerated (see Figure 1), which hinders epitaxy. On the contrary, Ni₈₀ features a similar diameter range (0.9–1.2 nm) for $E_{\text{adh}} \leq -0.43 \text{ eV}$, while showing a good contact between the nanotube wall and the nanoparticle. At larger diameters (1.3–1.6 nm $E_{\text{adh}} \geq -0.70 \text{ eV}$), this contact decreases, but it is still better than for Ni₃₂.

In addition, given the available thermal energy, a nanoparticle can evolve from one local minimum structure to another. For smaller nanoparticles, local minima are closer in energy,⁵¹ thus an easier transition from minimum to minimum may occur, with Ni₃₂ and Ni₈₀ readily moving from one minimum to another at a rate related to E_{adh} . Conversely, local minima for larger nanoparticles are more scattered,⁵¹ so such transition in Ni₁₆₀ does not occur as easily. Accordingly, Ni₁₆₀ shows irregular transition structures for longer times than Ni₃₂ and Ni₈₀, thus negatively affecting a possible template effect. On the other hand, the faster dynamics in Ni₃₂ may also hinder a template effect because nucleation of carbon structures has to continuously adapt to structural changes as Ni₃₂ switches among different local minimum structures. In this scenario, Ni₈₀ perhaps offers the best compromise for a template effect to occur, among the three studied sizes.

Interplay between Evolving Nanoparticle Structure and Nascent Carbon Nanostructures. It has been assumed in the preceding discussion that epitaxy between the nanotube and the nanoparticle does indeed occur. Although some authors have presented evidence correlating the structure of the nanoparticle of the nanotubes,^{19–21} it is still debatable whether the nanoparticle imposes its structure on the nascent nanotube (direct template effect) or the nanotube conditions the structure of the nanoparticle (inverse template effect) due to factors such as the higher strength of C–C bonds versus M–M bonds^{22,52} and the melting point depression of metallic nanoparticles.⁵³ We had previously suggested the

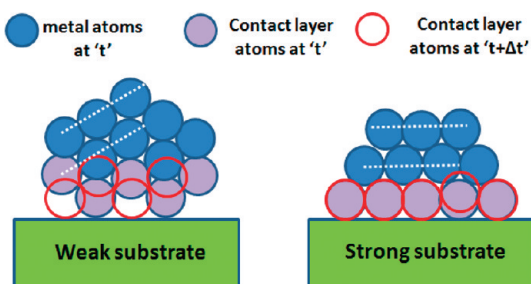


Figure 3. Side-view schematics capturing the most typical behavior of the nanoparticle structure for a weak interaction with the support and poor wetting (left) and a strong interaction with the support and good wetting (right). Metal atoms of the “contact layer” are represented by filled purple circles; regular metal atoms are represented by filled blue circles. The position of the atoms in the contact layer (unfilled red circles) after “ Δt ” picoseconds denotes a fast dynamics for the “weak substrate” and a slow dynamics for the “strong substrate”. The white dashed line corresponds to the [110] direction of the (111) facet shown.

use of a supported nanoparticle on a substrate with an adequate E_{adh} to solve this issue.²² We had also demonstrated through DFT calculations that if the fcc(111) facet is oriented such that the [110] direction (or the (100) plane) is at a 30° with respect to the substrate, carbon rings (and other structures) preferably adopted the armchair configuration but preferred the zigzag configuration when the angle is 0° .²² Trajectory analysis of our current simulations shows that, when the wetting is poor, the [110] direction is *usually* at 30° with respect to the substrate but *usually* at 0° when the wetting is good. Notice that a good wetting is caused by strong E_{adh} , which results in the nanoparticle featuring a flat “frozen” (111) epitaxial contact layer,³⁹ thus the natural packing sequence of the upper layers results in the formation of a (111) facet with the [110] direction parallel to the substrate. On the other hand, weak E_{adh} values result in poor wetting and an *uneven* mobile contact layer due to the up-and-down motion of the contact layer atoms. This behavior is somewhat transmitted to the upper layers, resulting in the [110] direction at an angle with the substrate. It must be noted that, due to the non-equilibrium nature of the nanotube growth process, this is only a general outline of the overall behavior of the nanoparticle during growth (schematized in Figure 3). Thus the nanoparticle can display “transient structures” contradicting the outlined trends. Nevertheless, according to the observed nanoparticle structural/dynamic trends and our previous DFT studies, we expect the probability for production of near-armchair nanotubes to increase at weaker values of E_{adh} and the probability for production of near-zigzag to increase at stronger values of E_{adh} , assuming upright growth ($\varphi_G \sim 90^\circ$). Interestingly, such trends appeared to be reproduced by Ni₃₂ and Ni₈₀, although $\varphi_G \neq 90^\circ$ throughout most of the simulations, thus indicating the need of a more detailed analysis.

It is useful to point out that, for the smallest particles, as E_{adh} increases, the shape of the nanoparticle changes from rounded (high wetting angle) to a flatter shape (low wetting angle). In the flatter shape (strong E_{adh}), the contact layer is flat and relatively still, with the atoms in upper layer positioning on the hollow sites of the layer underneath, favoring fcc packing, and the (110) surface direction parallel to the substrate (Figure 3, right). In the rounded shape (weak E_{adh}), the influence of the substrate is weaker, with a much more dynamic contact layer (Figure 3, left). Thus, the nanoparticle seems to adopt a structure of polyhedral character. This structural transition is evident for Ni₃₂ at $E_{\text{adh}} = -0.70$ and -1.39 eV. The influence of E_{adh} on this polyhedron fcc transition has been previously discussed.⁵⁴ Notice that the interaction with the support alters the nanoparticle structure, thus creating different scenarios for nanotube growth. Additionally, the same values of E_{adh} that favor fcc structures also notably slow down the nanoparticle dynamics, decreasing the rate of metal-mediated defect annealing, thus hindering a possible template effect.

Although weaker values of E_{adh} result in wetting values $\omega > 90^\circ$ that, in principle, favor a nanoparticle structure adequate for near-armchair growth for growing directions $\varphi_G = 90^\circ$, they also result in more mobile metal atoms than those found for stronger values of E_{adh} . Therefore, at weaker values of E_{adh} , the nanoparticle is expected to be more susceptible to inverse template effects than at stronger values of E_{adh} . Since it has been suggested that near-armchair nanotubes are favored thermodynamically and kinetically over near-zigzag ones,^{55–57} besides analyzing the existence of a substrate-assisted template effect, we also discuss whether such majority of near-armchair nanotubes found at weaker values of E_{adh} may result from such effect. This is carried out through a careful analysis of the simulation trajectories to correlate the nanoparticle structure and the nascent carbon structure, eventually, nanotube structure.

It has been demonstrated through DFT calculations ($T = 0$ K) that three-fold hollow sites on fcc(111) facets and four-fold hollow sites in fcc(100) facets are the most stable sites for carbon adsorption on transition metals such as Ni, Co, and Fe.^{58–61} It follows that the systematic occupation of these sites results in the formation of a graphene monolayer correlated to the underlying facet structure. Such correlation is the foundation for a potential template effect of the nanoparticle upon the nascent nanotube.^{19,22,49} However, it is important to recognize that at higher temperatures ($T = 1000$ K) this correlation could be hindered because carbon atoms possess enough energy to overcome diffusion barriers and are able to occupy other less preferred sites (e.g., bridge and top sites). Additionally, at higher temperatures, the surface of the nanoparticle is continuously evolving. Thus, a less optimal scenario

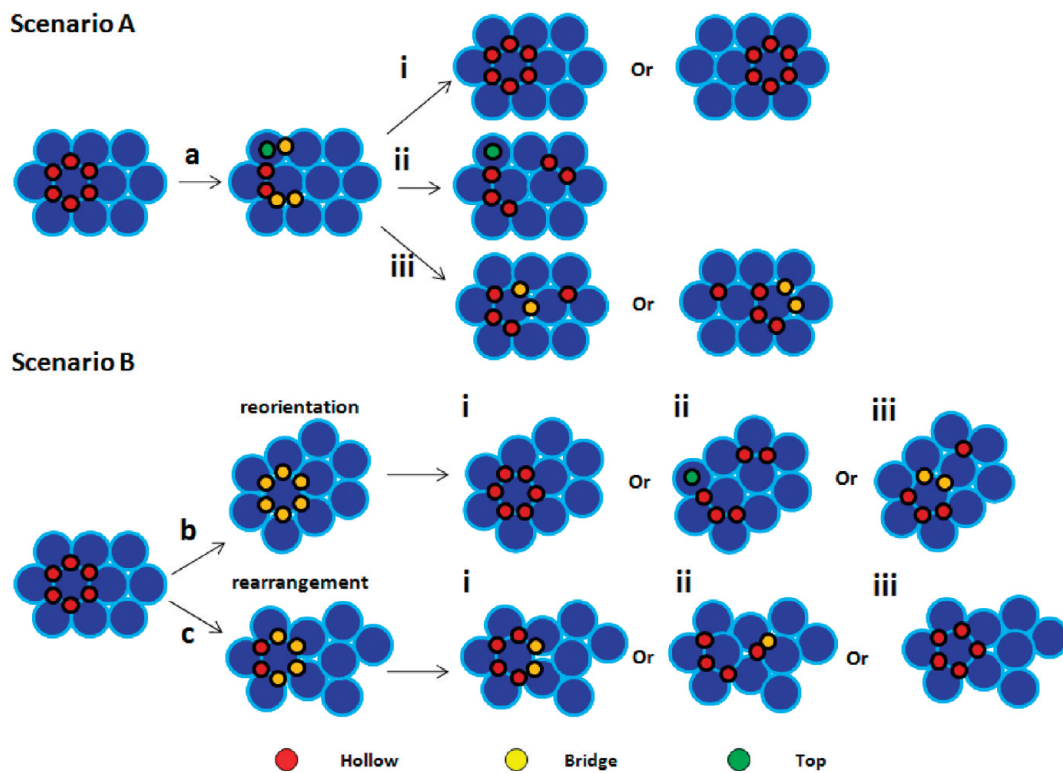


Figure 4. Schematics of a typical surface region in the nanoparticle, exemplifying general trends regarding the type of sites occupied and the correlation between the nanoparticle structure and the early formation of carbon rings. In scenario A (top), within a time interval Δt , the surface pattern and the matching ring are stable, then the ring breaks down (a). In scenario B (bottom), within a time interval Δt , the surface pattern and the matching ring are stable, then the surface pattern undergoes either a reorientation (b) or a rearrangement (c). Panels i through iii schematize typical configurations observed after either event a, b, or c occurs.

for epitaxy than that modeled in DFT calculations occurs. We begin the analysis of this high-temperature scenario looking at the interplay between the surface structure and the early formation of carbon rings (at simulation times $t < 1.0$ ns) on Ni_{32} , Ni_{80} , and Ni_{160} across various values of E_{adh} since E_{adh} affects the nanoparticle dynamics.

Figure 4 displays a summary representing some general trends gathered from the visual analysis of the trajectories. The figure is organized to demonstrate two different scenarios: the first (scenario A) where the surface is relatively stable and the carbon nanostructure needs to relocate for maximizing the occupancy of the most stable sites; in the second (scenario B), the surface is able to restructure and rearrange and the carbon nanostructures follow these motions. The main observations are as follows: (1) Early rings displayed short lifetimes τ ($\tau < 25.0$ ps), wherein pentagonal rings generally appear earlier but have shorter lifetimes than hexagonal ones. (2) Both hexagonal and pentagonal rings display higher stability (i.e., longer lifetimes) when such rings match the underlying surface structure, with a perfect matching corresponding to all of the ring atoms occupying hollow positions (Figure 4) and a good matching still occurring when more than half of the ring atoms occupy hollow positions. The interaction of the nanoparticle with these hollow

atoms appears to determine the orientation of the ring on the nanoparticle surface (e.g., Figure 4sA,a-i, where the nomenclature indicates scenario A as sA and the respective pathway a-i). Thus, hexagonal rings usually are centered on metal atoms possessing six surface nearest neighbors, such as in a fcc(111) facet (e.g., Figure 4sA,a-i), whereas pentagonal rings tend to do so on metal atoms possessing five surface nearest neighbors (e.g., Figure 4sB,c-iii). (3) There are time intervals of steady regions, wherein the nanoparticle surface region maintained its structure, and a hexagonal or pentagonal ring is able to match the underlying surface pattern (i.e., most atoms occupying hollow positions). Due to thermal fluctuations, this carbon structure may be altered, and the ring breaks down, with most carbon atoms no longer occupying hollow positions (Figure 4sA,a) for a few picoseconds (e.g., $\tau < 3$ ps). This is followed by any of the following events as pictured in Figure 4sA: (i) the original ring is recovered on the original (or a different) surface location (Figure 4sA,a-i); (ii) the carbon atoms rearrange into a chain(s), with most of them occupying hollow positions (Figure 4sA,a-ii); or (iii) the original hexagonal (or pentagonal) ring is not recovered, but a new pentagonal (or hexagonal) ring is formed on the original (or a different) surface location, with most atoms occupying hollow positions (Figure 4sA,a-iii). (4) A different

scenario (Figure 4sB) occurs when the matching between the surface and the ring is altered because of changes of the surface structure, instead of the ring being broken down. Nonetheless, this surface restructuring destabilizes the ring since most of its carbon atoms are no longer occupying hollow sites (*i.e.*, matching no longer occurs) as a result of either surface reorientation (Figure 4sB,b) or rearrangement (Figure 4sB,c). Thus the ring structure only holds for a short time (*e.g.*, $\tau < 3$ ps) before any of the following events occurs: (i) the ring *does not* break down but reorients to match the new surface orientation (Figure 4sB,b/c-i); or (ii) the ring *does* break down with the carbon atoms rearranging into structures matching the new surface geometry (Figure 4sB,b/c-ii/iii).

It must be noted that, due to the effect of E_{adh} on the nanoparticle mobility, scenario A (Figure 4) was observed to dominate at stronger E_{adh} and larger nanoparticle sizes, whereas scenario B (Figure 4) was observed to dominate at weaker E_{adh} and smaller nanoparticle sizes. It is also noteworthy that, in similar way as carbon structures that matched the underlying surface appeared to be more stable than the ones that did not, nanoparticle (surface) regions supporting matching structures appeared to be more stable (and better defined) than those that did not. This was evidenced in the simulations through observation of the behavior of “carbon-free” surface regions in comparison to “carbon-covered” surface regions during time intervals where epitaxial matching occurred. This may be interpreted as a cooperative effect between carbon and metal, wherein the *template effect* contributes to the stability of carbon structures, whereas the *inverse template effect* contributes to the stability of metal surface regions. It follows from the mobility– E_{adh} relation that this cooperative effect is more important at weaker E_{adh} and smaller nanoparticles. However, notice that (at least) at this early stage the template effect dominates since analysis of the simulation trajectories shows that the carbon atoms usually rearrange following pattern changes in the nanoparticle surface but seldom vice versa.

Template Effect at High Temperatures. Figure S5 (Supporting Information) and Figure 5 (top) illustrate combinations of the scenarios described in Figure 4 for relatively low E_{adh} values. A first case involves Ni₃₂ and $E_{\text{adh}} = -0.16$ eV (Figure S5), where an existing Y-shaped C₆ chain rearranges to form a pentagonal ring (branched) on a *defective* fcc(111) facet. Since the matching was non-optimal, a sequence of events consistent with scenarios A and B illustrates the cooperative stabilization between carbon nanostructures and the metal surface with the formation of a hexagonal ring accurately matching a *perfect* fcc(111) facet. This is maintained despite the reorientation of the latter, consistently with scenario B-b in Figure 4. At the slightly higher $E_{\text{adh}} = -0.26$ eV (Figure 4, top) an H-shaped C₁₁

chain preceded the formation of a four-branched pentagonal ring. This ring, centered on a five-coordinated metal atom (see Figure 4sB,c-iii), was shortly destabilized due to thermal fluctuations but recovered and stabilized during 10.0 ps (scenario A,a-i in Figure 4). However, when a surface rearrangement no longer favors the pentagonal ring, a hexagonal one is formed instead (scenario B,c-iii in Figure 4), with 4/6 of the ring atoms in hollow positions, exemplifying how the carbon nanostructures try to follow the evolving surface structure. Also notice that for both E_{adh} values, configurations dominated by occupation of hollow sites last longer ($\tau > 15.0$ ps) than those where this does not occur ($\tau < 3.0$ ps).

The described scenarios (Figure 4) can also be mapped onto the actual nanoparticle surfaces for stronger interactions for which the metal atoms appear less mobile. For $E_{\text{adh}} = -0.43$ eV (Figure S5) and -0.70 (Figure 5), H-shaped C₉ and C₁₂ chains preceded the ring formation, respectively. For the former case, the surface did not show major changes for 29.5 ps, thus stabilizing a branched hexagonal ring, with carbon atoms preferably occupying hollow sites (scenario A). Moreover, new atoms are incorporated to the ring branches without destabilizing the existing matching. After this time, the surface rearranged, disrupting the matching and breaking the ring (scenario B,c-ii in Figure 4). For $E_{\text{adh}} = -0.70$ eV (Figure 5, middle), the surface mobility is further reduced, which allows a strained fcc(111) region to survive for 12.0 ps, supporting a moderately matching branched pentagonal ring for 7.0 ps, after which a hexagonal ring is formed. The strained region evolves into a fcc(111) region, finally allowing the ring to fully occupy hollow sites. Notice that the preference of ring atoms for hollow sites is observed even during the short-lived ($\tau = 2.0$ ps) transitional five-fold surface configuration. Interestingly, the formation of an additional ring was also observed, which can be related to the formation of the graphene network. Initially, the ring was a pentagonal one following the pattern of the surface but morphed into a hexagonal one following a surface pattern rearrangement. It must be noted that all of the atoms of the newly formed ring were located in hollow sites, but as a result, since the two rings are connected, the five atoms of the first ring previously occupying hollow sites were displaced. This exemplifies how *lattice mismatching* between the metal and graphene walls can prevent a dominant occupation of hollow sites as the graphene network starts to form. Nonetheless, it must also be noted that, despite the resulting offset of the first ring with respect to the surface pattern, the zigzag direction of both rings and the fcc ⟨110⟩ surface direction appeared aligned. This suggests that a template effect could occur without the occupation of hollow sites being absolutely dominant. Nonetheless, the occupation of hollow sites still appears to be a key

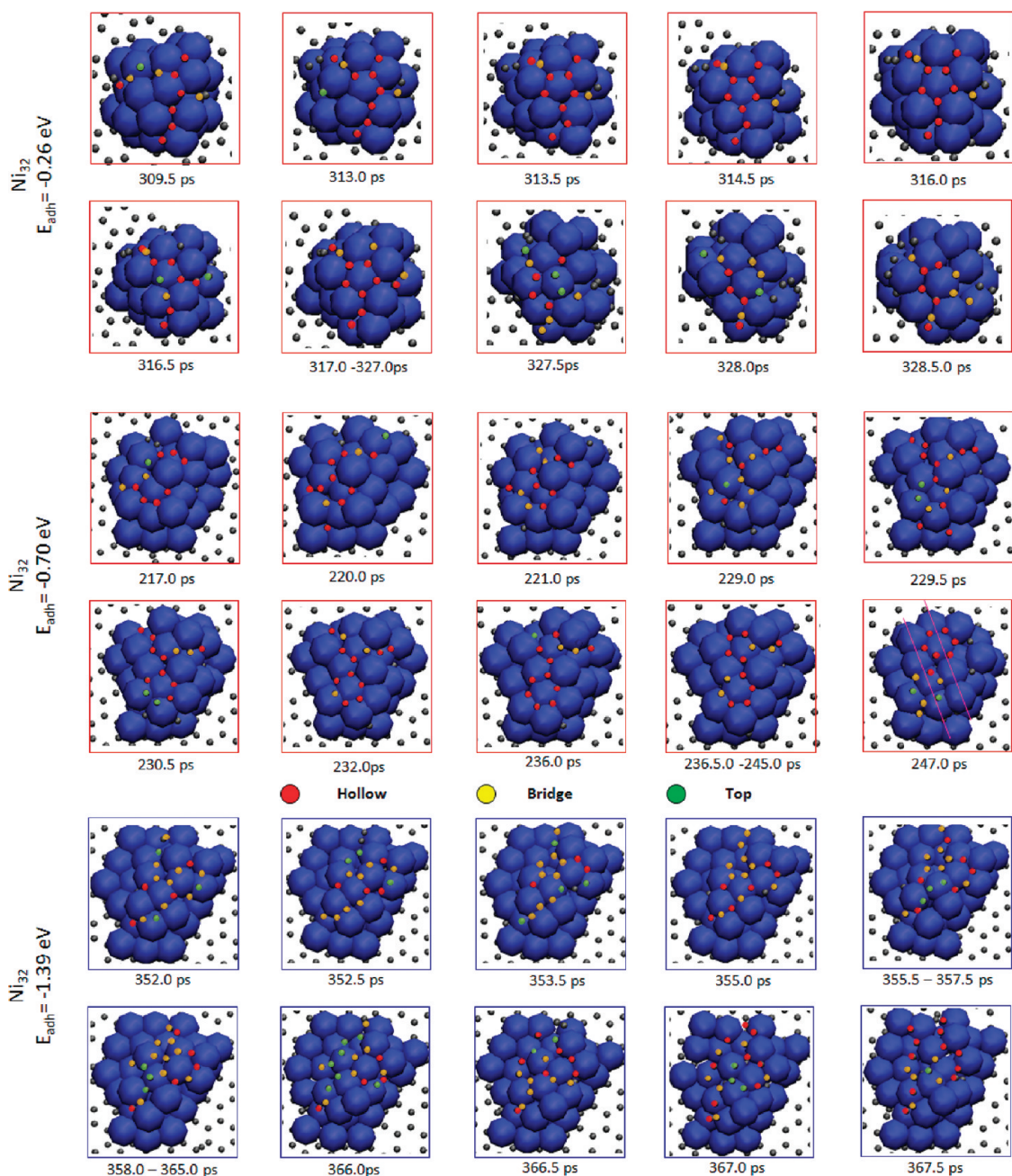


Figure 5. Simulation frames showing the initial formation of ring structures on a supported Ni_{32} nanoparticle for three different metal/substrate interactions: $E_{\text{adh}} = -0.26 \text{ eV}$ (top), $E_{\text{adh}} = -0.70 \text{ eV}$ (middle), and $E_{\text{adh}} = -1.39 \text{ eV}$ (bottom). The relevant carbon atoms are colored according to the type of site they occupy on the nanoparticle surface: hollow (red), bridge (yellow), or top (green).

factor because the orientation of the graphene network is to be influenced by the orientation of individual rings adsorbing on hollow sites since carbon atoms attach more strongly to the surface on such sites.

Although a strong metal/substrate interaction reduces the mobility of the surface, for the simulations using the strongest values of E_{adh} (-1.39 eV), it was more difficult to observe the correlation between the surface pattern and the early ring formation. Figure 5 (bottom) shows that a C_{16} structure containing a heptagonal ring preceded the formation of a pentagonal

ring. Such ring formed concatenated to the heptagonal ring. In a short time span ($\tau \approx 10.0 \text{ ps}$), an additional (concatenated) ring is formed and transformed into a hexagonal ring. However, during this time span, the occupation of hollow sites does not dominate since there is a similar occupation of bridge sites and hollow sites. Interestingly, after this time, the pentagonal and hexagonal rings break down, whereas the heptagonal ring was observed to remain stable, demonstrating the difficulty in annealing this kind of defects if E_{adh} is too strong.

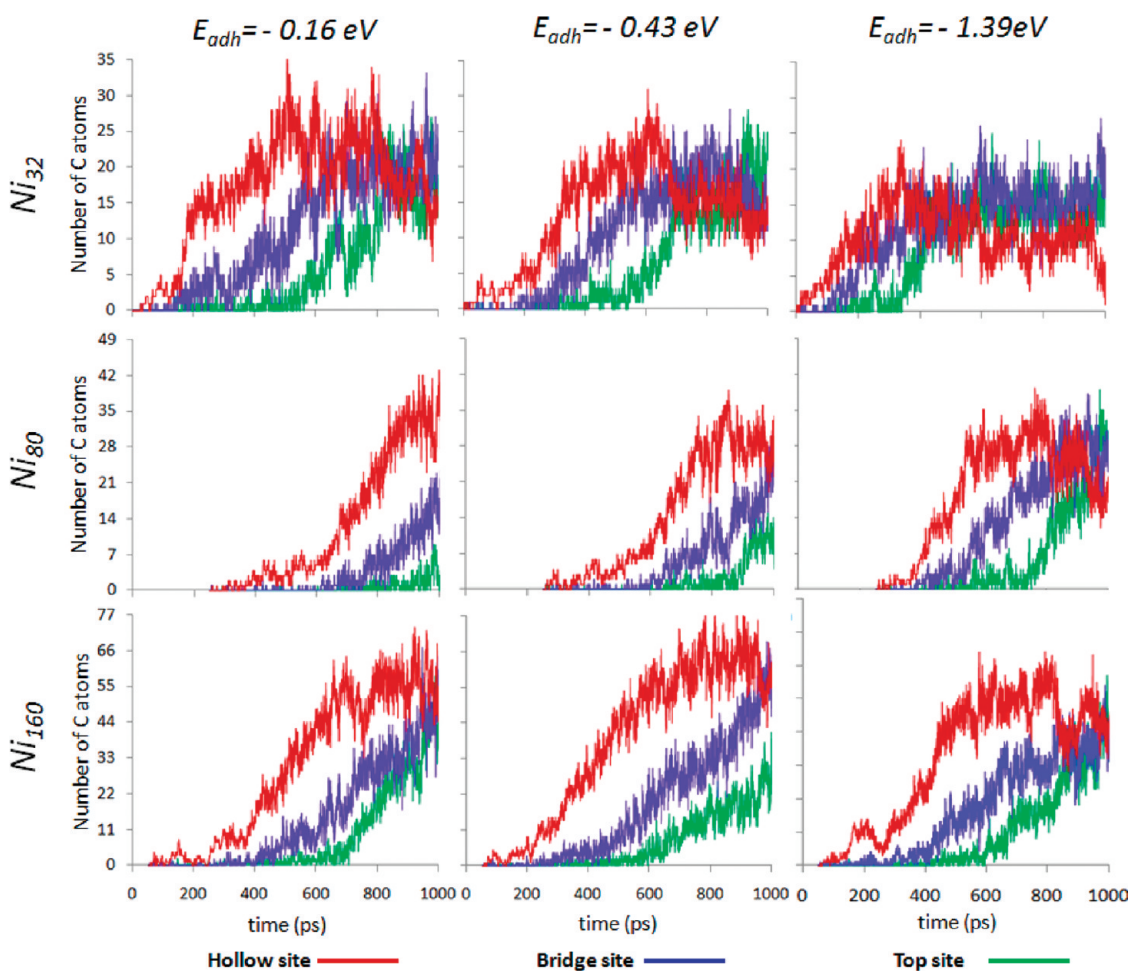


Figure 6. Plots showing the number of carbon atoms occupying each type of site on the nanoparticle vs time.

Dynamics of the Adsorption Occupancies at Nucleation Stages.

Similar findings to the ones described for Ni_{32} are also encountered for Ni_{80} and Ni_{160} , such as the involvement of a larger number of atoms for the formation of the first ring as E_{adh} increases, and the important role of the occupation of hollow sites in the correlation between the surface structure and the nascent carbon nanostructure. Figure 6 shows the number of carbon atoms occupying hollow, bridge, and top sites at various E_{adh} values for Ni_{32} , Ni_{80} , and Ni_{160} during the initial 1000 ps of simulation. According to the analyses of the simulation trajectories, this time interval corresponds to the formation of the nanotube cap preceding the lift-off. It can be observed that the occupation of hollow sites dominates in the initial stages of the simulations, wherein ~70% of the atoms adsorbed on the surface occupy hollow sites, whereas the remaining ~30% adsorb typically on bridge sites and to a lesser extent on top sites. This is in agreement with the relative adsorption site preference calculated by DFT.^{58–61} In an ideal scenario, 100% of the atoms would adsorb on hollow sites in such a way that the pattern of the hollow sites on the surface would determine the geometry of the nascent carbon nanostructures.

However, this does not occur due to the high temperature, which allows carbon atoms to occupy a variety of sites, and because of the dynamic structure of the nanoparticle, which does not *rigorously* match the graphene wall of the nanotube due to curvature effects, a time-dependent surface structure, surface imperfections, and lattice mismatching. Nevertheless, Figure 6 shows an initial ~70% occupancy of hollow sites, indicating that there still is an important influence of the nanoparticle on the geometry of nucleating structures. After a certain time, the percentage of atoms in hollow, bridge, and top positions becomes equal, ~33%. This transition to a more random distribution occurs at earlier times as the value E_{adh} increases and as the nanoparticle size decreases. For instance, for Ni_{32} , this occurs after ~600 ps for $E_{adh} = -0.16$ and -0.43 eV, whereas it occurs after ~300 ps for $E_{adh} = -1.39$ eV, in agreement with the results discussed in Figure 5 and Figure S5. On the other hand, for $E_{adh} = -1.39$ eV, this transition occurs after ~300 ps for Ni_{32} , after ~800 ps for Ni_{80} , and after ~1000 ps for Ni_{160} .

Observation of the simulation trajectories at the transition times shows that such transition to a random distribution of site occupancies coincides with the

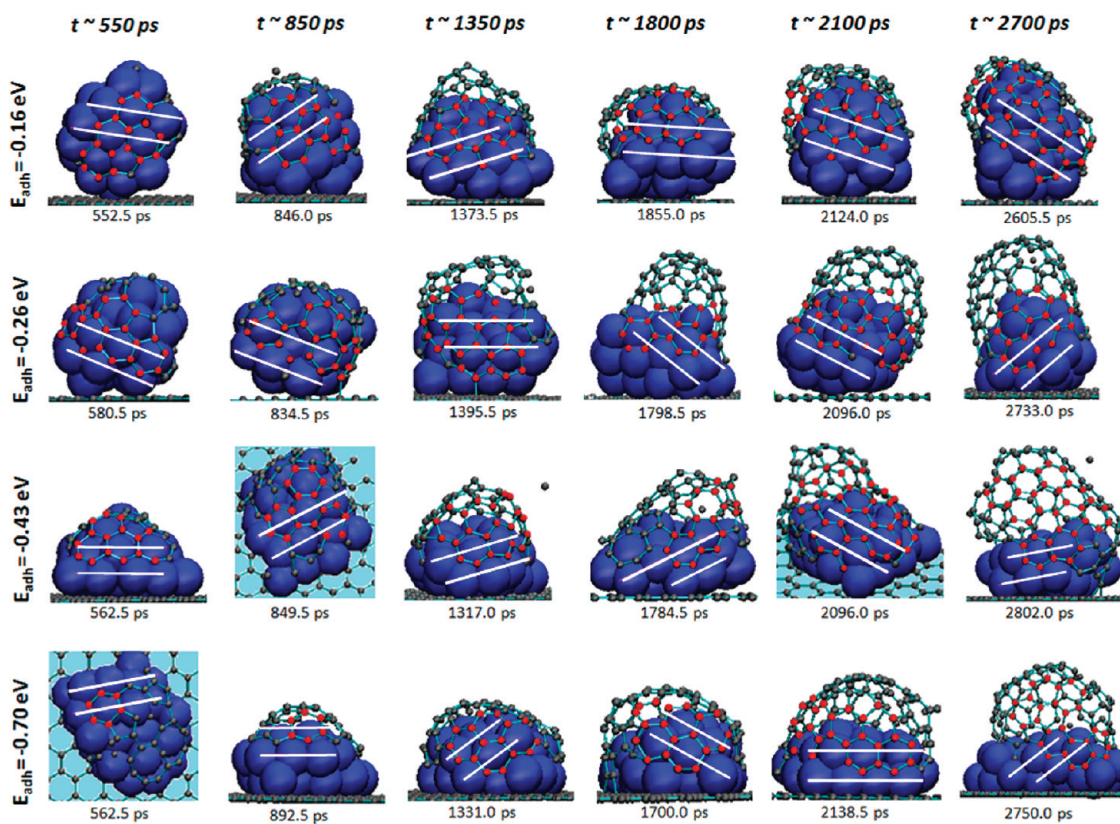


Figure 7. Snapshots showing the correlation between the $\langle 110 \rangle$ direction in the Ni_{32} nanoparticle and the orientation of the nascent nanotube graphene network at different simulation times.

formation of a graphene network on the surface. This is consistent with the occurrence of lattice mismatching, as discussed for $E_{\text{adh}} = -0.70$ eV in Figure 5. The results presented in Figures 5 and 6 also demonstrate the importance of atom mobility for the growth of defect-free matching structures as occurs for the growth on thin films.⁶² If the conditions are such that carbon atoms are not very mobile, it is more difficult for the atoms to move toward the most stable sites, thus facilitating the formation of carbon nanostructures not matching the underlying surface. These structures tend to be defective. For instance, we noticed that the formation of rings with more than six atoms (e.g., a decagonal ring) became more common as E_{adh} approached -1.39 eV. Moreover, the reduced mobility also hinders the annealing of these defective rings, therefore decreasing the quality of the nanotube structure. On the other hand, the presence of defective rings in the graphene network amplifies the lattice mismatching further hindering the occurrence of a template effect.

Correlation between Facet Structure and Nanotube Rim Structure at End of Nucleation/Beginning of Carbon Nanotube Growth. Although lattice mismatching may occur, as the decrease in occupation of hollow sites at the end of nucleation shows in Figure 6, there may still be a correlation between the structures of the nanoparticle and the nascent nanotube, as shown in Figure 5 for

$E_{\text{adh}} = -0.70$ eV. Accordingly, we observed the simulation trajectories to analyze whether such correlation was found or not. The results of Ni_{32} simulations are shown in Figure 7 (Ni_{80} and Ni_{160} cases are shown in Figures S6 and S7) for various E_{adh} values at different times. The $\langle 110 \rangle$ direction on the nanoparticle surface is denoted by a white solid line. It is observed that the orientation of such direction can vary during the simulation in a manner consistent with scenario B,b in Figure 4. Although not clearly seen in Figure 7 due to the limited number of simulation frames shown, analysis of the trajectories reveals that the $\langle 110 \rangle$ direction is frequently parallel to the substrate for stronger E_{adh} values, whereas such direction is frequently found at $\sim 30^\circ$ with respect to the substrate for weaker E_{adh} values. This correlates well with the change in the wetting pattern with E_{adh} . It must be noted that the change in orientation of the $\langle 110 \rangle$ direction occurs faster for weaker E_{adh} values due to a higher atom mobility.

Additionally, Figure 7 suggests that indeed there seems to be a correlation between the orientation of the $\langle 110 \rangle$ direction of the surface and the zigzag direction on the graphene wall. This occurs with some of the rings having their atoms occupying hollow sites, whereas adjacent rings have their atoms occupying other sites, or even not clearly occupying a specific site. It is apparent that the rings matching the surface

pattern through occupation of hollow sites strongly influence the orientation of the graphene network. Broadening the analysis of early ring formation further in the simulation, it is found that scenarios analogous to those discussed in Figure 4 are also encountered once the graphene network has formed. For instance, the graphene network may temporarily mismatch the underlying surface but return to a matching position after a short time (scenario A). Also, the underlying surface may change, resulting in a temporary mismatch, which makes the network to reorient in order to maintain the matching (scenario B). However, it is important to recognize that, as the nanotube cap forms and the graphene network grows in size, the events occurring in one nanoparticle region are connected to those occurring elsewhere. For instance, matching of a region of nascent graphene network with a nanoparticle region may conflict with matching with another region. Thus the matching in one region may be lost to accommodate matching on another one depending on which one is more energetically favorable. Therefore, it can be inferred in agreement with DFT results^{59–61} that the graphene network is oriented to increase the number of atoms occupying hollow sites.

As a result of the nanotube/nanoparticle dynamics, there are time intervals where matching between the nanotube and the nanoparticle becomes unclear, even when these time frames are located between intervals where the correlation is apparent. It must be noted that the correlation between the hexagonal graphene network and the nanoparticle surface also suffers due to the presence of pentagonal or heptagonal (and other) rings, which tend to align their center on top of a metal atom, but preventing neighbor hexagonal rings to orientate “correctly”. Since increasing E_{adh} results in nanotubes of lesser quality, it is also observed that the nanotube/nanoparticle correlation is more difficult to observe for stronger E_{adh} values. In Figure 7, it can be observed for $t \sim 550$ ps that the number of hexagonal rings matching the surface decreases from four to one as E_{adh} changes from -0.16 to -0.70 eV. As the simulations progress, some of these defects heal, but with more difficulty as E_{adh} increases, as previously discussed. Thus, the intervals during which the correlation can be observed are longer as E_{adh} is decreased. Similar trends are observed for simulations of Ni_{80} and Ni_{160} (Figures S6 and S7). Notice that, since the size of the graphene network increases with the nanoparticle size, the percentage of carbon atoms that clearly matches the surface decreases because the number of defects increases (given that for the same time scale it is easier to anneal a smaller network). Similarly, although a larger nanoparticle offers more contact area, it also increases the probability of existence of conflicting regions (due to high temperature dynamics) for the graphene network to match. Thus, for Ni_{160} , the intervals at which the

correlation is observed are noticeably shorter than for Ni_{32} and Ni_{80} .

It also follows from the previous discussion that for a particular time not all of the entire graphene network matches the nanoparticle structure (due to either the graphene structure or the nanoparticle structure). On the other hand, as mentioned earlier, the graphene region around the nanotube rim is observed to be very dynamic regarding bond breaking and formation mediated by the dynamics of metal atoms. This occurs in such a way that the rim region constantly follows the nanoparticle surface pattern in a similar way as observed for early ring formation. This means that the rim region is continuously rearranging in an effort to match the underlying structure even though this may cause a mismatch elsewhere. This is explained on the basis of the lower coordination of the rim atoms, requiring less bonds to be rearranged in order to modify their positions, and to the stronger interaction of these carbon atoms with metal atoms according to DFT calculations and incorporated into the force field used in the simulation.²⁵ Thus, it is inferred that, energetically, a good matching around the rim, but not optimal elsewhere, is preferred over a good matching elsewhere, but not optimal around the rim. Therefore, the contact between the nanotube rim region and the nanoparticle appears to play an important role for both template effect and defect annealing. Accordingly, the lower number of atoms involved in the nanotube/nanoparticle matching as E_{adh} increases may result from the comparatively poorer contact between the nanotube rim and the nanoparticle. Also, the poorer contact of the rim region with the nanoparticle as E_{adh} increases may hinder the influence of the catalyst structure on that of the nanotube. On the other hand, decreasing E_{adh} may increase the effect of the nanoparticle structure provided that such metal/substrate interaction is strong enough to hinder an inverse template effect.

SUMMARY AND CONCLUSIONS

Instantaneous catalysis accelerated simulated nanotube growth, reducing the quality of the nanotubes grown, but allowed us to perform a large number of simulations at reasonable computational times. Analyses of the simulation trajectories showed nanotube growth to occur through the stages of (i) carbon dissolution, (ii) carbon segregation, (iii) formation of chains and rings, (iv) cap formation, (v) cap lift-off, and (vi) growth. Cap lift-off appeared to occur faster for strong E_{adh} values because capillary effects (*i.e.*, nanoparticle stretching inside the nanotube) were not as important as for weak E_{adh} values. Also, at strong E_{adh} values, the nanotubes appeared to grow more defective, which is consistent with lower atom mobility hindering annealing. The growth direction tended to be at a low angle with respect to the substrate for

strong E_{adh} values, at a right angle for moderate, and at varying angle for weak E_{adh} .

The final nanotube structures were analyzed to evaluate the chiral angle θ_c , which was determined to be high (near-armchair) or low (near-zigzag). The largest nanoparticles did not present a clear trend regarding θ_c versus E_{adh} , but the smallest and the intermediate size did. Interestingly, the intermediate size presented a more defined trend than the smallest one. This suggested a compromise between reducing the nanoparticle size to limit the number of possible chiralities (*i.e.*, indirect chiral control) and increasing the nanoparticle size to improve contact with the nanotube walls, thus resulting in an optimum intermediate nanoparticle size for chirality control. Further details regarding the effect of the nanoparticle structure were explored through analysis of the formation of early rings and the correlation of the $\langle 110 \rangle$ surface direction and the nascent nanotube (graphene) wall orientation.

The occupation of hollow sites on the nanoparticle surface appeared as a key factor for establishing a nanotube/nanoparticle structural correlation. Our analysis showed a preference for this site despite the available thermal energy and the nanoparticle dynamics. This was clear during the early ring formation, wherein near 70% of the carbon atoms were shown to occupy such sites. It was shown that early carbon structures attempt to follow the underlying surface structure, even for weak E_{adh} values, as described by scenarios A and B. Nevertheless, a cooperative

dynamics between the nascent structures and the nanoparticle was observed where the template effect stabilized the nascent structures and the inverse template effect stabilized the underlying surface, even though the former was observed to dominate.

Upon cap nucleation, lattice mismatching effects become important, and the occupation of hollow sites drops. However, it was still possible to correlate the structures of the nascent network/nanotube and the nanoparticle (Figure 6 and Figures S6 and S7). This correlation was more difficult to observe as E_{adh} increased because of more defective network (due to low mobility and more difficult annealing) and poorer contact (decrease of capillary effects). On the other hand, this correlation was easier to observe in the intermediate nanoparticle because of a better contact with the nanotube than that of the smallest nanoparticle and a less conflictive matching than that offered by the largest one (due to conflicting domains orientation on the nanoparticle surface). Additionally, the nanotube rim region in contact with the nanoparticle appears more active than other nanotube regions since it was observed to continuously anneal in an effort to follow the nanoparticle structure (*i.e.*, occupy hollow sites), thus impacting the orientation of the graphene network in rest of the tube. These results support the hypothesis that the catalyst structure affects the nanotube structure, thus encouraging further experimental and theoretical efforts to find the conditions at which this effect can be maximized.

METHODS

Classical reactive molecular dynamics using the SIMCAT code is used to simulate the growth of carbon nanotubes on supported nanoparticles.²⁵ Three metallic clusters, namely, Ni₃₂, Ni₈₀, and Ni₁₆₀, were used to study the influence of the nanoparticle size. Magic size clusters characterized for their unusually high cohesive energy and highly symmetric structure have been reported for 13, 55, and 147 atoms in unsupported nickel clusters, while 32, 81, and others are secondary magic sizes.⁶³ However, for supported nanoparticles, the interaction with the substrate may alter the given sizes as reported in the literature.^{64,65} In the present work, the clusters display different structural behavior for the various values of E_{adh} , but they never appear to adopt perfectly symmetric geometries, thus behaving as regular clusters. The nanoparticles are placed on a model substrate, whose interaction with the nanoparticle can be modified through the increase or decrease of a damping factor in the force field. The force field describes the most relevant interactions in the nanotube growth including: (1) metal–metal (MM) interactions, represented using the Sutton Chen potential;⁶⁶ (2) carbon–carbon (CC) interactions, characterized by a modified potential²⁵ inspired in the second generation reactive empirical bond order (REBO) Brenner potential;⁶⁷ (3) metal–carbon (MC) interactions, described using a Tersoff–Brenner scheme,²⁵ wherein the strength of the interaction depends on the hybridization of the carbon atoms and the local geometry of the metal atoms; for instance, on the basis of density functional theory (DFT) calculations,²⁵ the interaction between carbon atoms at the nanotube tip (sp^2 atoms) and metal is modeled weaker than the interaction between carbon atoms at the nanotube rim (sp atoms) and metal; (4) carbon–substrate

interactions are described using equivalent expressions to those for CC interactions, but using a different damping factor; (5) metal–substrate interactions are described using equivalent expressions to those for MC interactions, but different parameterization. A detailed description of the force field equation can be found elsewhere.²⁵ This force field has been proven useful to get insights on the nanotube growth and to determine how the interplay of the different interactions promotes either nanotube growth or encapsulation for supported and unsupported nanoparticles as a function of temperature, nanoparticle size, and strength of metal–substrate interactions.^{37–39}

At the beginning of the simulations, the nanoparticle is located at the center of a tetragonal simulation box, whose dimensions are $c = 84.0 \text{ \AA}$ and $a = b = 25.0 \text{ \AA}$ for Ni₃₂ and Ni₈₀, and 39 \AA for Ni₁₆₀. Precursor atoms initially appear in the gas phase at random positions according to the desired density ($0.0001 \text{ atoms}/\text{\AA}^3$). The number of precursor atoms is such that a preset gas density is maintained, and they move inside the simulation box according to the simulation temperature. When “by chance” a precursor atom contacts the nanoparticle, it is instantaneously converted into a carbon atom and new precursor atoms appear at a random position in the gas phase. Thus, there is neither a predetermined carbon addition rate of carbon nor predetermined addition sites on the nanoparticle. There are no interactions between a precursor atom and either metal, carbon, or substrate atoms. However, when a precursor atom travels closer than 1.0 \AA to a metal atom, it irreversibly transforms into a carbon atom whose interactions with the rest of the system are described accordingly. For all sizes, the number of carbon atoms dissolved inside the nanoparticle reaches a maximum within 500 ps. However, it must be noted

that segregation to the surface was observed before this “super-saturation” occurs. This algorithm models an instantaneous irreversible catalysis, thus accelerating the growth with respect to experimental rates.⁶⁸ The temperature is set at 1000 K, which is representative of CVD growth,^{13,15,69} and separately rescaled to the target temperature for each species. The parameters used in our simulations result in the following interaction energies: (i) carbon–carbon ~ -5.0 eV, (ii) sp^2 -carbon–metal ~ -0.10 eV, (iii) sp -carbon–metal ~ -2.78 eV, (iv) carbon–substrate $\sim -1 \times 10^{-5}$ eV, (v) metal–substrate interaction E_{adh} takes different values, namely, -0.10 , -0.16 , -0.43 , -0.70 , and -1.39 eV. Typical values for E_{adh} range from -0.14 to -0.62 eV for metal supported on MgO and -2.47 eV for metal supported on SrTiO₃.^{70,71} We note that a number of factors can affect the interaction strength between nanoparticle and substrate. For instance, E_{adh} can change with the nanoparticle size/shape in a nonmonotonic fashion⁷² and can be affected by structural defects on the support⁷³ or by the presence of functional groups on the support surface.⁷⁴ However, some trends can be observed for commonly utilized supports such as silica, magnesia, and graphene. Namely, adsorption on silica tends to be stronger than on magnesia but weaker than on graphene, as revealed by E_{adh} values (per contact atom) of -1.1 ,⁷² -0.23 ,⁷⁵ and -2.07 eV⁷³ for Au₅ clusters on silica, magnesia, and graphene, respectively. On the other hand, calculation of E_{adh} for one metal atom on silica⁷⁶ shows Ni ($E_{adh} = -1.90$ eV) to adsorb more strongly than Fe ($E_{adh} = -1.70$ eV), but more weakly than Co ($E_{adh} = -2.20$ eV). However, on magnesia,⁷⁷ Ni adsorbs more strongly ($E_{adh} = -1.32$ eV) than both Fe ($E_{adh} = -0.91$ eV) and Co ($E_{adh} = -0.81$ eV). Increasing the number of metal atoms, the value of E_{adh} (per contact atom) decreases. In silica, the trend is maintained with $E_{adh} = -0.62$ and -0.34 eV for Co and Ni, respectively,⁷⁸ but not so in magnesia with $E_{adh} \sim -0.67$ and -0.63 eV for Co and Ni, respectively.⁷⁹ On the other hand, the relative values of CC and MC interactions agree well with previous DFT calculations.²² The length of each simulation is 5.0 ns, which allows one to observe the stages of dissolution, cap nucleation, and cap lift-off. A simulation step of 0.5 fs is used. The trajectory is saved so each trajectory frame represents 0.5 ps of simulation. The trajectories were analyzed using VMD.⁸⁰

For each determination of chiral angle, the axial direction of the growing carbon nanotube is first established using VMD.⁸⁰ The final trajectory frame is rotated to obtain the “best” view of the nanotube cross section. Then a straight line passing through two axis points is drawn, and the system is rotated to obtain the true length view of this line. Finally, according to the orientation of the hexagonal pattern of the growing nanotube relative to this line, the chiral angle (θ_c) is estimated as high (between 15 and 30°) or low (between 0 and 15°). On the other hand, to count the number of C atoms occupying a given surface site type, a utility program was created to identify the atoms on the surface and classify them using the carbon–metal coordination number as criteria. For instance, carbon atoms with one metal neighbor are said to occupy *top* sites, whereas those with two metal neighbors occupy *bridge* sites, or those with three or four metal neighbors occupy *hollow* sites.

The simulation statistics were improved by using different initial conditions for the catalytic nanoparticle; the different initial structures were varied as a function of five distinct annealing times (t_a). During the catalyst preparation in CVD growth, usually a precursor oxide undergoes a calcination/reduction/annealing process, which generates the metallic nanoparticles that catalyze the nanotube growth. The time frames utilized in these stages can be controlled in order to modify the catalyst characteristics. For instance, the catalyst precursor can be partially reduced to control the particle size.¹⁶ In a CVD experiment, the structure/diameter of the reduced nanoparticles, before growth, is unlikely to be identical. Thus, here the different annealing times are used *only* to represent the diversity of initial catalytic structures.

Acknowledgment. Financial support from the Department of Energy, Basic Energy Sciences, Grant DE-FG02-06ER15836, and from TAMU-CONACYT Grant 2011-2 is gratefully acknowledged.

This research used resources of the National Energy Research Scientific Computing Center, which is supported by the Office of Science of the U.S. Department of Energy under Contract No. DE-AC03-76SF00098, and from TAMU Supercomputer Center. Use of the Center for Nanoscale Materials supported by the U.S. Department of Energy, Office of Science, Office of Basic Energy Sciences, under Contract No. DE-AC02-06CH11357 is also acknowledged.

Supporting Information Available: Snapshots of growing nanotubes as a function of time for various E_{adh} and three nanoparticle sizes with Figures S1–S4 representing different annealing times for the nanocatalyst particle; initial formation of ring structures for Ni₃₂ and weak E_{adh} (Figure S5); snapshots showing the correlation between the $\langle 110 \rangle$ direction in the Ni₈₀ and the orientation of the nascent nanotube graphene network at different simulation times (Figure S6) and for Ni₁₆₀ (Figure S7). This material is available free of charge via the Internet at <http://pubs.acs.org>.

REFERENCES AND NOTES

- Marvin, L. *Nanotubes C. Nanoscience, and Nanotechnology. Mater. Sci. Eng., C* **2001**, *15*, 1–11.
- Baughman, R. H.; Zakhidov, A. A.; de Heer, W. A. *Carbon Nanotubes—The Route toward Applications. Science* **2002**, *297*, 787–792.
- Polizzi, S.; Savadogo, O.; Poulin, P.; Yahia, L. H. *Applications of Carbon Nanotubes-Based Biomaterials in Biomedical Nanotechnology. J. Nanosci. Nanotechnol.* **2006**, *6*, 1883–1904.
- Dresselhaus, M. S.; Dresselhaus, G.; Eklund, P. C. *Science of Fullerenes and Carbon Nanotubes: Their Properties and Applications*; Elsevier Science: San Diego, CA, 1996.
- Postma, H. W. C.; Teepen, T.; Yao, Z.; Grifoni, M.; Dekker, C. *Carbon Nanotube Single-Electron Transistors at Room Temperature. Science* **2001**, *293*, 76–79.
- Byrne, M. T.; Gun'ko, Y. K. *Recent Advances in Research on Carbon Nanotube–Polymer Composites. Adv. Mater.* **2010**, *22*, 1672–1688.
- Yu, X.; Munge, B.; Patel, V.; Jensen, G.; Bhirde, A.; Gong, J. D.; Kim, S. N.; Gillespie, J.; Gutkind, J. S.; Papadimitrakopoulos, F.; et al. *Carbon Nanotube Amplification Strategies for Highly Sensitive Immunodetection of Cancer Biomarkers. J. Am. Chem. Soc.* **2006**, *128*, 11199–11205.
- Wilder, J. W. G.; Venema, L. C.; Rinzler, A. G.; Smalley, R. E.; Dekker, C. *Electronic Structure of Atomically Resolved Carbon Nanotubes. Nature* **1998**, *391*, 59–62.
- Ajayan, P. M.; Lambert, J. M.; Bernier, P.; Barbedette, L.; Collie, C.; Planeix, J. M. *Growth Morphologies during Cobalt-Catalyzed Single-Shell Carbon Nanotube Synthesis. Chem. Phys. Lett.* **1993**, *215*, 509–517.
- Thess, A.; Lee, R.; Nikolaev, P.; Dai, H.; Petit, P.; Robert, J.; Xu, C.; Lee, Y. H.; Kim, S. G.; Rinzler, A. G.; et al. *Crystalline Ropes of Metallic Carbon Nanotubes. Science* **1996**, *273*, 483–487.
- Zheng, M.; Jagota, A.; Semke, E. D.; Diner, B. A.; McLean, R. S.; Lustig, S. R.; Richardson, R. E.; Tassi, N. G. *DNA-Assisted Dispersion and Separation of Carbon Nanotubes. Nat. Mater.* **2003**, *2*, 338–342.
- Krupke, R.; Hennrich, F.; von Löhneysen, H.; Kappes, M. M. *Separation of Metallic from Semiconducting Single-Walled Carbon Nanotubes. Science* **2003**, *301*, 344–347.
- Lolli, G.; Zhang, L.; Balzano, L.; Sakulchaicharoen, N.; Tan, Y.; Resasco, D. E. *Tailoring (n,m) Structure of Single-Walled Carbon Nanotubes by Modifying Reaction Conditions and the Nature of the Support of CoMo Catalysts. J. Phys. Chem. B* **2006**, *110*, 2108–2115.
- Telalovic, S.; Ramanathan, A.; Mul, G.; Hanefeld, U. *TUD-1: Synthesis and Application of a Versatile Catalyst, Carrier, Material. J. Mater. Chem.* **2010**, *20*, 642–658.
- Wang, H.; Wang, B.; Quek, X.-Y.; Wei, L.; Zhao, J.; Li, L.-J.; Chan-Park, M. B.; Yang, Y.; Chen, Y. *Selective Synthesis of (9,8) Single Walled Carbon Nanotubes on Cobalt Incorporated TUD-1 Catalysts. J. Am. Chem. Soc.* **2010**, *132*, 16747–16749.

16. He, M. S. A.; Chernov, A. I.; Fedotov, P. V.; Obraztsova, E. D.; Rikkinen, E.; Zhu, Z.; Sainio, J.; Jiang, H.; Nasibulin, A. G.; Kauppinen, E. I.; et al. Selective Growth of SWNTs on Partially Reduced Monometallic Cobalt Catalyst. *Chem. Commun.* **2011**, *47*, 1219–1221.
17. He, M. S. A.; Chernov, A. I.; Obraztsova, E. D.; Sainio, J.; Rikkinen, E.; Jiang, H.; Zhu, Z.; Kaskela, A.; Nasibulin, A. G.; Kauppinen, E. I.; et al. Low Temperature Growth of SWNTs on a Nickel Catalyst by Thermal Chemical Vapor Deposition. *Nano Res.* **2011**, *4*, 334–342.
18. He, M.; Chernov, A. I.; Fedotov, P. V.; Obraztsova, E. D.; Sainio, J.; Rikkinen, E.; Jiang, H.; Zhu, Z.; Tian, Y.; Kauppinen, E. I.; et al. Predominant (6,5) Single-Walled Carbon Nanotube Growth on a Copper-Promoted Iron Catalyst. *J. Am. Chem. Soc.* **2010**, *132*, 13994–13996.
19. Zhu, H.; Suenaga, K.; Wei, J.; Wang, K.; Wu, D. A Strategy To Control the Chirality of Single-Walled Carbon Nanotubes. *J. Cryst. Growth* **2008**, *310*, 5473–5476.
20. Chiang, W.-H.; Mohan Sankaran, R. Linking Catalyst Composition to Chirality Distributions of As-Grown Single-Walled Carbon Nanotubes by Tuning $\text{Ni}_x\text{Fe}_{1-x}$ Nanoparticles. *Nat. Mater.* **2009**, *8*, 882–886.
21. Harutyunyan, A. R.; Chen, G.; Paronyan, T. M.; Pigos, E. M.; Kuznetsov, O. A.; Hewaparakrama, K.; Kim, S. M.; Zakharov, D.; Stach, E. A.; Sumanasekera, G. U. Preferential Growth of Single-Walled Carbon Nanotubes with Metallic Conductivity. *Science* **2009**, *326*, 116–120.
22. Gomez-Gualdrón, D. A.; Zhao, J.; Balbuena, P. Nanocatalyst Structure as a Template To Define Chirality of Nascent Single-Walled Carbon Nanotubes. *J. Chem. Phys.* **2011**, *134*, 014705.
23. Hofmann, S.; Sharma, R.; Ducati, C.; Du, G.; Mattevi, C.; Cepek, C.; Cantoro, M.; Pisana, S.; Parvez, A.; Cervantes-Sodi, F.; et al. *In Situ* Observations of Catalyst Dynamics during Surface-Bound Carbon Nanotube Nucleation. *Nano Lett.* **2007**, *7*, 602–608.
24. Moseler, M.; Cervantes-Sodi, F.; Hofmann, S.; Csányi, G. b.; Ferrari, A. C. Dynamic Catalyst Restructuring during Carbon Nanotube Growth. *ACS Nano* **2010**, *4*, 7587–7595.
25. Martinez-Limia, A.; Zhao, J.; Balbuena, P. Molecular Dynamics Study of the Initial Stages of Catalyzed Single-Wall Carbon Nanotubes Growth: Force Field Development. *J. Mol. Model.* **2007**, *13*, 595–600.
26. Shibuta, Y.; Maruyama, S. Molecular Dynamics Simulation of Formation Process of Single-Walled Carbon Nanotubes by CCVD Method. *Chem. Phys. Lett.* **2003**, *382*, 381–386.
27. Ding, F. Molecular Dynamics Study of the Catalyst Particle Size Dependence on Carbon Nanotube Growth. *J. Chem. Phys.* **2004**, *121*, 2775.
28. Ding, F.; Rosén, A.; Bolton, K. Dependence of SWNT Growth Mechanism on Temperature and Catalyst Particle Size: Bulk versus Surface Diffusion. *Carbon* **2005**, *43*, 2215–2217.
29. Zhao, J.; Martinez-Limia, A.; Balbuena, P. B. Understanding Catalysed Growth of Single-Wall Carbon Nanotubes. *Nanotechnology* **2005**, *16*, S575–S581.
30. Balbuena, P. B.; Zhao, J.; Huang, S.; Wang, Y.; Sakulchaicharoen, N.; Resasco, D. E. Role of the Catalyst in the Growth of Single-Wall Carbon Nanotubes. *J. Nanosci. Nanotechnol.* **2006**, *6*, 1247–1258.
31. Raty, J.-Y.; Gygi, F.; Galli, G. Growth of Carbon Nanotubes on Metal Nanoparticles: A Microscopic Mechanism from *Ab Initio* Molecular Dynamics Simulations. *Phys. Rev. Lett.* **2005**, *95*, 096103.
32. Amara, H.; Bichara, C.; Ducastelle, F. Understanding the Nucleation Mechanisms of Carbon Nanotubes in Catalytic Chemical Vapor Deposition. *Phys. Rev. Lett.* **2008**, *100*, 056105.
33. Ohta, Y.; Okamoto, Y.; Page, A. J.; Irle, S.; Morokuma, K. Quantum Chemical Molecular Dynamics Simulation of Single-Walled Carbon Nanotube Cap Nucleation on an Iron Particle. *ACS Nano* **2009**, *3*, 3413–3420.
34. Page, A. J.; Yamane, H.; Ohta, Y.; Irle, S.; Morokuma, K. QM/MD Simulation of SWNT Nucleation on Transition-Metal Carbide Nanoparticles. *J. Am. Chem. Soc.* **2010**, *132*, 15699–15707.
35. Page, A. J.; Ohta, Y.; Irle, S.; Morokuma, K. Mechanisms of Single-Walled Carbon Nanotube Nucleation, Growth, and Healing Determined Using QM/MD Methods. *Acc. Chem. Res.* **2010**, *43*, 1375–1385.
36. Neyts, E. C.; Shibuta, Y.; van Duin, A. C. T.; Bogaerts, A. Catalyzed Growth of Carbon Nanotube with Definable Chirality by Hybrid Molecular Dynamics–Force Biased Monte Carlo Simulations. *ACS Nano* **2010**, *4*, 6665–6672.
37. Ribas, M. A.; Ding, F.; Balbuena, P. B.; Yakobson, B. I. Nanotube Nucleation versus Carbon-Catalyst Adhesion-Probed by Molecular Dynamics Simulations. *J. Chem. Phys.* **2009**, *131*, 224501.
38. Burgos, J. C.; Reyna, H.; Yakobson, B. I.; Balbuena, P. B. Interplay of Catalyst Size and Metal–Carbon Interactions on the Growth of Single-Walled Carbon Nanotubes. *J. Phys. Chem. C* **2010**, *114*, 6952–6958.
39. Burgos, J. C.; Jones, E.; Balbuena, P. B. Effect of the Metal–Substrate Interaction Strength on the Growth of Single-Walled Carbon Nanotubes. *J. Phys. Chem. C* **2011**, *115*, 7668–7675.
40. Bandow, S.; Asaka, S.; Saito, Y.; Rao, A. M.; Grigorian, L.; Richter, E.; Eklund, P. C. Effect of the Growth Temperature on the Diameter Distribution and Chirality of Single-Wall Carbon Nanotubes. *Phys. Rev. Lett.* **1998**, *80*, 3779.
41. Okamoto, A.; Shinohara, H. Control of Diameter Distribution of Single-Walled Carbon Nanotubes Using the Zeolite-CCVD Method at Atmospheric Pressure. *Carbon* **2005**, *43*, 431–436.
42. Rümmeli, M. H.; Kramberger, C.; Schäffel, F.; Borowiak-Palen, E.; Gemming, T.; Rellinghaus, B.; Jost, O.; Löffler, M.; Ayala, P.; Pichler, T.; et al. Catalyst Size Dependencies for Carbon Nanotube Synthesis. *Phys. Status Solidi B* **2007**, *244*, 3911–3915.
43. Gavillet, J.; Loiseau, A.; Journet, C.; Willaime, F.; Ducastelle, F.; Charlier, J. C. Root-Growth Mechanism for Single-Wall Carbon Nanotubes. *Phys. Rev. Lett.* **2001**, *87*, 275504.
44. Page, A. J.; Ohta, Y.; Okamoto, Y.; Irle, S.; Morokuma, K. Defect Healing during Single-Walled Carbon Nanotube Growth: A Density-Functional Tight-Binding Molecular Dynamics Investigation. *J. Phys. Chem. C* **2009**, *113*, 20198–20207.
45. Pigos, E.; Penev, E. S.; Ribas, M. A.; Sharma, R.; Yakobson, B. I.; Harutyunyan, A. R. Carbon Nanotube Nucleation Driven by Catalyst Morphology Dynamics. *ACS Nano* **2011**, *10*, 1021/rn2040457.
46. Bower, C. Nucleation and Growth of Carbon Nanotubes by Microwave Plasma Chemical Vapor Deposition. *Appl. Phys. Lett.* **2000**, *77*, 2767.
47. Bengaard, H. S.; Nørskov, J. K.; Sehested, J.; Clausen, B. S.; Nielsen, L. P.; Molenbroek, A. M.; Rostrup-Nielsen, J. R. Steam Reforming and Graphite Formation on Ni Catalysts. *J. Catal.* **2002**, *209*, 365–384.
48. Swart, J. C. W.; van Steen, E.; Ciobica, I. M.; van Santen, R. A. Interaction of Graphene with FCC-Co(111). *Phys. Chem. Chem. Phys.* **2009**, *11*, 803–807.
49. Saadi, S.; Abild-Perdersen, F.; Helveg, S.; Sehested, J.; Hinnemann, B.; Appel, C. C.; Nørskov, J. K. On the Role of Metal Step-Edges in Graphene Growth. *J. Phys. Chem. C* **2010**, *114*, 11221.
50. Kunstrmann, J.; Quandt, A.; Boustani, I. An Approach To Control the Radius and the Chirality of Nanotubes. *Nanotechnology* **2007**, *18*, 155703.
51. Doye, J. P. K.; Calvo, F. Entropic Effects on the Structure of Lennard-Jones Clusters. *J. Chem. Phys.* **2002**, *116*, 8307–8317.
52. Zhu, W.; Börjesson, A.; Bolton, K. DFT and Tight Binding Monte Carlo Calculations Related to Single-Walled Carbon Nanotube Nucleation and Growth. *Carbon* **2010**, *48*, 470–478.
53. Qi, W. H. Size Effect on Melting Temperature of Nanosolids. *Phys. B: Condens. Matter* **2005**, *368*, 46–50.
54. Jiang, A. Q.; Awasthi, N.; Kolmogorov, A. N.; Setyawati, W.; Börjesson, A.; Bolton, K.; Harutyunyan, A. R.; Curtarolo, S. Theoretical Study of the Thermal Behavior of Free and Alumina-Supported Fe-C Nanoparticles. *Phys. Rev. B* **2007**, *75*.

55. Reich, S.; Li, L.; Robertson, J. Structure and Formation Energy of Carbon Nanotube Caps. *Phys. Rev. B* **2005**, *72*, 165423.
56. Gómez-Gualdrón, D. A.; Balbuena, P. B. The Role of Cap Chirality in the Mechanism of Growth of Single-Wall Carbon Nanotubes. *Nanotechnology* **2008**, *19*, 485604.
57. Ding, F.; Harutyunyan, A. R.; Yakobson, B. I. Dislocation Theory of Chirality-Controlled Nanotube Growth. *Proc. Natl. Acad. Sci. U.S.A.* **2009**, *106*, 2506–2509.
58. Jiang, D. E.; Carter, E. A. Carbon Atom Adsorption on and Diffusion into Fe(110) and Fe(100) from First Principles. *Phys. Rev. B* **2005**, *71*, 045402.
59. Cinquini, F.; Delbecq, F.; Sautet, P. A DFT Comparative Study of Carbon Adsorption and Diffusion on the Surface and Subsurface of Ni and Ni₃Pd Alloy. *Phys. Chem. Chem. Phys.* **2009**, *11*, 11546–11556.
60. Ramirez-Caballero, G. E.; Burgos, J. C.; Balbuena, P. B. Growth of Carbon Structures on Stepped (211) Cobalt Surfaces. *J. Phys. Chem. C* **2009**, *113*, 15658–15666.
61. Wang, Q.; Lim, K.; Yang, S.-W.; Yang, Y.; Chen, Y. Atomic Carbon Adsorption on Ni Nanoclusters: A DFT Study. *Theor. Chem. Acc.* **2011**, *128*, 17–24.
62. Park, S.; Clark, B. L.; Keszler, D. A.; Bender, J. P.; Wager, J. F.; Reynolds, T. A.; Herman, G. S. Low-Temperature Thin-Film Deposition and Crystallization. *Science* **2002**, *297*, 65.
63. Hu, W. J.; Mei, L. M.; Li, H. Simulation of Ground State Structure of Nickel Clusters ($n \leq 40$). *Solid State Commun.* **1996**, *100*, 129–131.
64. Zhang, P.; Xie, Y. Q.; Zhang, W. X.; Ning, X. J.; Zhuang, J. Different Magic Number Behaviors in Supported Metal Clusters. *J. Nanopart. Res.* **2011**, *13*, 1801–1807.
65. Rossi, G.; Anghinolfi, L.; Ferrando, R.; Nita, F.; Barcaro, G.; Fortunelli, A. Prediction of the Structures of Free and Oxide-Supported Nanoparticles by Means of Atomistic Approaches: The Benchmark Case of Nickel Clusters. *Phys. Chem. Chem. Phys.* **2010**, *12*, 8564–8570.
66. Sutton, A. P.; Chen, J. Long-Range Finnis–Sinclair Potentials. *Philos. Mag. Lett.* **1990**, *61*, 139–146.
67. Brenner, D. W.; Shenderova, O. A.; Harrison, J. A.; Stuart, S.; Ni, B.; Sinnott, S. B. Second-Generation A Reactive Empirical Bond Order (REBO) Potential Energy Expression for Hydrocarbons. *J. Phys.: Condens. Matter* **2002**, *14*, 783.
68. Yao, Y.; Liu, R.; Zhang, J.; Jiao, L.; Liu, Z. Raman Spectral Measuring of the Growth Rate of Individual Single-Walled Carbon Nanotubes. *J. Phys. Chem. C* **2007**, *111*, 8407–8409.
69. Bachilo, S. M.; Strano, M. S.; Kittrell, C.; Hauge, R. H.; Smalley, R. E.; Weisman, R. B. Structure-Assigned Optical Spectra of Single-Walled Carbon Nanotubes. *Science* **2002**, *298*, 2361–2366.
70. Pacchioni, G. Supported Nickel and Copper Clusters on MgO(100): A First Principles Calculation on the Metal/Oxide Interface. *J. Chem. Phys.* **1996**, *104*, 7329.
71. Robach, O.; Renaud, G.; Barbier, A. Structure and Morphology of the Ag/MgO(001) Interface during *In Situ* Growth at Room Temperature. *Phys. Rev. B* **1999**, *60*, 5858.
72. Veith, G. M.; Lupini, A. R.; Rashkeev, S.; Pennycook, S. J.; Mullins, D. R.; Schwartz, V.; Bridges, C. A.; Dudney, N. J. Thermal Stability and Catalytic Activity of Gold Nanoparticles Supported on Silica. *J. Catal.* **2009**, *262*, 92–101.
73. Pulido, A.; Boronat, M.; Corma, A. Theoretical Investigation of Gold Clusters Supported on Graphene Sheets. *New J. Chem.* **2011**, *35*, 2153–2161.
74. Meyer, R.; Ge, Q. F.; Lockemeyer, J.; Yeates, R.; Lemanski, M.; Reinalda, D.; Neurock, M. An *Ab Initio* Analysis of Adsorption and Diffusion of Silver Atoms on Alumina Surfaces. *Surf. Sci.* **2007**, *601*, 134–145.
75. Molina, L. M.; Hammer, B. Theoretical Study of CO Oxidation on Au Nanoparticles Supported by MgO(100). *Phys. Rev. B* **2004**, *69*.
76. Ma, Q. S.; Klier, K.; Cheng, H. S.; Mitchell, J. W. Interaction Between Catalyst and Support. 4. Periodic Trends and Patterns in Interactions of First-Row Transition Metals with the Silica Surface. *J. Phys. Chem. B* **2002**, *106*, 10121–10127.
77. Fernandez, S.; Markovits, A.; Minot, C. Adsorption of the First Row of Transition Metals on the Perfect and Defective MgO(100) Surface. *Chem. Phys. Lett.* **2008**, *463*, 106–111.